Spectroscopic and Computational Investigation of Room-Temperature Decomposition of a Chemical Warfare Agent Simulant on Polycrystalline Cupric Oxide

Lena Trotochaud,[†] Roman Tsyshevsky,[‡] Scott Holdren,[§] Kenan Fears,[||] Ashley R. Head,[†] Yi Yu,[†,§] Osman Karslıoğlu,[†] Sven Pletincx,[†,⊥] Bryan Eichhorn,[§] Jeffrey Owrutsky,[||] Jeffrey Long,[||] Michael Zachariah,[§] Maija M. Kuklja,[‡] and Hendrik Bluhm*[,†,#]

[†]Chemical Sciences Division, Lawrence Berkeley National Laboratory, Berkeley, California 94720, United States

[‡]Materials Science and Engineering Department, University of Maryland, College Park, Maryland 20742, United States

[§]Department of Chemistry and Biochemistry, University of Maryland, College Park, Maryland 20742, United States

[||]Chemistry Division, U.S. Naval Research Laboratory, Washington, DC 20375, United States

[⊥]SURF Research Group, Department of Materials and Chemistry, Vrije Universiteit Brussel, Pleinlaan 2, 1050 Brussels, Belgium

[#]Advanced Light Source, Lawrence Berkeley National Laboratory, Berkeley, California 94720, United States

S *Supporting Information*

ABSTRACT: Certain organophosphorus molecules are infamous due to their use as highly toxic nerve agents. The filtration materials currently in common use for protection against chemical warfare agents were designed before organophosphorus compounds were used as chemical weapons. A better understanding of the surface chemistry between simulant molecules and the individual filtration-material components is a critical precursor to the development of more effective materials for filtration, destruction, decontamination, and/or sensing of nerve agents. Here, we report on the surface adsorption and reactions of a sarin simulant molecule, dimethyl methylphosphonate (DMMP), with cupric oxide surfaces. *In situ* ambient pressure X-ray photoelectron and infrared

in situ spectroscopy + theory

spectroscopies are coupled with density functional calculations to propose mechanisms for DMMP decomposition on CuO. We find extensive room temperature decomposition of DMMP on CuO, with the majority of decomposition fragments bound to the CuO surface. We observe breaking of PO–CH₃, P–OCH₃, and P–CH₃ bonds at room temperature. On the basis of these results, we identify specific DMMP decomposition mechanisms not seen on other metal oxides. Participation of lattice oxygen in the decomposition mechanism leads to significant changes in chemical and electronic surface environment, which are manifest in the spectroscopic and computational data. This study establishes a computational baseline for the study of highly toxic organophosphorous compounds on metal oxide surfaces.
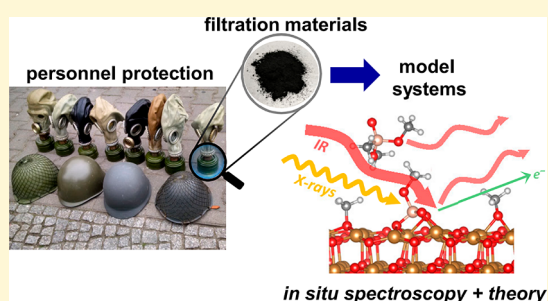
1. INTRODUCTION

Organophosph(on)ates with the general formula O=P(OR)-(OR′)(R″) and their derivatives are small molecules whose relative toxicities can be tailored by modifying the substituent functional groups. Their utility as pesticides and herbicides has thus become widespread.[1] More infamously, certain organophosphonates were developed as the G- and V-series chemical warfare agents (CWAs), which irreversibly interrupt function of the acetylcholinesterase (AChE) enzyme.[1–4] Despite broad international condemnation of CWA use, the relative ease of obtaining precursor compounds and carrying out CWA syntheses results in their continued appearance in the commission of terrorist attacks (e.g., 1994 and 1995, GB, attacks in Matsumoto and Tokyo), war crimes (e.g., 2013−2017, GB, Syrian civil war), and assassinations (2017, VX, Kim Jong-nam). Thus, protection against CWA exposure is unfortunately a persistent need for civilian, medical, and military personnel, and

numerous studies have been and are being undertaken to explore the chemical mechanisms of CWA destruction, decontamination, and sensing.[1,5−8]

Air filtration systems are the first line of defense for personnel protection against CWAs. The most widely used material in gas-mask filters for commercial, industrial, and military applications is ASZM-TEDA, a high surface area composite of porous, activated carbon adsorbent impregnated with triethylenediamine (TEDA) and compounds (presumably oxides) of Cu ('A'), Ag ('S'), Zn ('Z'), and Mo ('M').[9] While gas-mask filters containing ASZM-TEDA provide temporary, broad-spectrum protection against many toxic agents, little is known about the fundamental chemistry of organophosphonate adsorption/decomposition on

 7483

the individual metal oxide components.[9] Noncatalytic decomposition of organophosphonate nerve agents on the metal oxide components may block active sites or could inadvertently yield other toxic, volatile compounds that could penetrate the filter. Thus, a detailed understanding of the surface chemistry of metal oxides in the presence of organophosphonates is required for the design of more effective filtration materials and a more robust understanding of failure mechanisms in current materials.[1]

The acute toxicity of CWAs introduces an extra layer of complexity to *in situ* studies of filtration materials, and requires that, in many laboratory settings, a less toxic simulant molecule is substituted for a particular CWA of interest. Dimethyl methylphosphonate (DMMP, Figure 1) is a widely studied
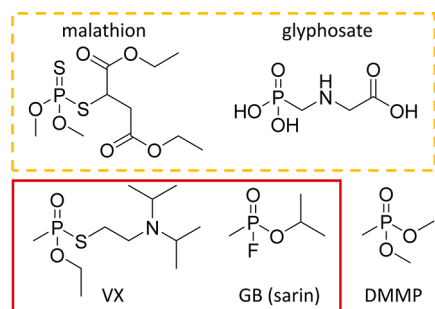
Figure 1. Examples of organophosph(on)ate derivatives used as pesticides/herbicides (inside dashed line) and nerve agents (inside solid line). DMMP is used in this study as a simulant molecule for sarin.

simulant molecule that has been shown to effectively mimic sarin (GB) adsorption during filter life testing.[9] Removal of the highly labile P—F bond eliminates the AChE inhibiting properties of sarin, while the other functional groups (phosphoryl, methyl, and alkoxy) are retained in DMMP. This makes DMMP an effective simulant for CWA adsorption (through the P=O moiety), but the lack of the P—F bond makes it unclear whether DMMP decomposition on any particular metal oxide surface effectively mimics CWA decomposition on that same surface.[8] Thus, studies which provide experimentally validated computational benchmarks will enable a more complete mechanistic understanding of organophosphonate decomposition on metal oxides and are critical precursors for informing the study of live agents. Detailed information on the chemical mechanism of DMMP decomposition on different oxide surfaces is still lacking, as such a holistic approach to studying these systems (especially for composite materials) is inherently complex.

In situ spectroscopic analysis in the presence of gas molecules is required for a comprehensive understanding of organophosphonate adsorption and decomposition under relevant atmospheric conditions. Ambient pressure X-ray photoelectron spectroscopy (APXPS) allows for collection of chemically specific information about decomposition products and changes to the metal oxide surface during exposure to one or more gas-phase compounds. Traditional *ex situ* XPS studies of various surfaces after exposure to DMMP have been reported previously;[10−16] however, they may suffer from enhanced desorption of weakly bound species under UHV conditions. We have recently demonstrated the efficacy of *in situ* APXPS combined with density functional theory (DFT) in examining the adsorption of DMMP on MoO₃ surfaces.[17] MoO₃ was shown to be relatively inert with regard to DMMP, since the thermodynamically stable, oxygen-terminated surface lacks under-coordinated metal atom sites to initiate DMMP

adsorption[18,19] Introducing surface defects and hydroxyl groups was shown to greatly increase DMMP adsorption and decomposition on MoO₃.[17]

In this work, we link APXPS, diffuse-reflectance Fourier-transform infrared spectroscopy (DRIFTS), and DFT to investigate the adsorption and decomposition of DMMP on polycrystalline cupric oxide (CuO) surfaces, as a simplified model for the copper component of ASZM-TEDA. The monoclinic structure of CuO gives rise to abundant under-coordinated metal centers to facilitate DMMP adsorption. In contrast to many other metal oxide surfaces, we see significant decomposition of DMMP at room temperature on CuO. Specifically, we observe the formation of methoxy groups on the CuO surface in DRIFTS and a decrease in the number of P—CH₃ bonds, both of which are confirmed by APXPS and DFT. Quantitative analysis of APXPS spectra also indicates that both P—OCH₃ and P—CH₃ bonds are breaking and Cu—OCH₃ and O—CH₃ bonds are forming on the CuO surface. The participation of CuO lattice oxygen atoms (O_{lat}) in the formation of Cu—O_{lat}—P and O_{lat}—CH₃ bonds is supported by the mechanism proposed on the basis of DFT calculations, and also leads to noteworthy changes in the photoelectron spectra of the CuO substrate, indicating changes in the electronic structure which extend throughout the several layers of CuO probed with XPS. APXPS and FTIR data were interpreted with the aid of DFT to propose two mechanisms for DMMP decomposition involving either PO—CH₃ bond breaking or sequential P—OCH₃ and P—CH₃ bond breaking. Room temperature P—CH₃ bond breaking on metal oxides is rare, and PO—CH₃ bond scission has not previously been reported at room temperature on any other metal oxide.

2. EXPERIMENTAL SECTION

2.1. FTIR Spectroscopy. All FTIR spectra were collected on Nicolet spectrometers equipped with liquid N₂ cooled MCT-A detectors. CuO nanopowder (<50 nm particle size) and DMMP (≥97.0% GC) were purchased from Sigma-Aldrich and used as received. A Harrick Scientific Praying Mantis DRA optical accessory was used with an associated Harrick Scientific high temperature reaction chamber HVCDRP-5 for the DRIFTS measurements. The CuO nanopowder was heated in 20 mL min⁻¹ of O₂ in the HVC chamber at 450 °C for 1 h prior to the DMMP exposure. The DMMP exposure was performed using a bubbler with Ar as the carrier gas. A flow rate of 25 mL min⁻¹ was used with an estimated DMMP concentration of 200 ppm (0.15 Torr). DRIFTS spectra were collected at 4 cm⁻¹ resolution in 1 min intervals by averaging 100 spectral scans every min. Complementary headspace analysis was performed by placing 100 mg of CuO or MoO₃ in a Harrick Scientific 10 cm gas cell under a N₂ atmosphere. After sealing the cell, 20 μL of DMMP was injected into the cell through a rubber septum. FTIR spectra were then collected (0.5 cm⁻¹ resolution) of the headspace above the powder at 10 min intervals; spectra were averaged over the first 3 min (108 scans) followed by a 7 min delay.

2.2. APXPS and NEXAFS. *In situ* ambient pressure XPS (APXPS) and near-edge X-ray absorption fine structure (NEXAFS) experiments were performed at the APXPS-1 end station[20] of beamline 11.0.2[21] at the Advanced Light Source at Lawrence Berkeley National Laboratory. The end station has designated chambers for sample preparation and sample analysis. The base pressure of both chambers was 5 × 10⁻⁹ Torr or lower. The entrance from the analysis chamber to the differentially pumped electrostatic lens system[22] of the electron energy analyzer is a conical aperture with a diameter of 0.2 mm; this configuration enables *in situ* measurements up to pressures of several Torr. DMMP (>97%, Fluka) was degassed via freeze−pump−thaw cycles (3×) and was introduced into the analysis chamber via a high-precision leak valve. The equilibrium vapor pressure of DMMP at 20 °C is 0.114 Torr.[23] In our previous work, we observed spectral contributions from gas phase
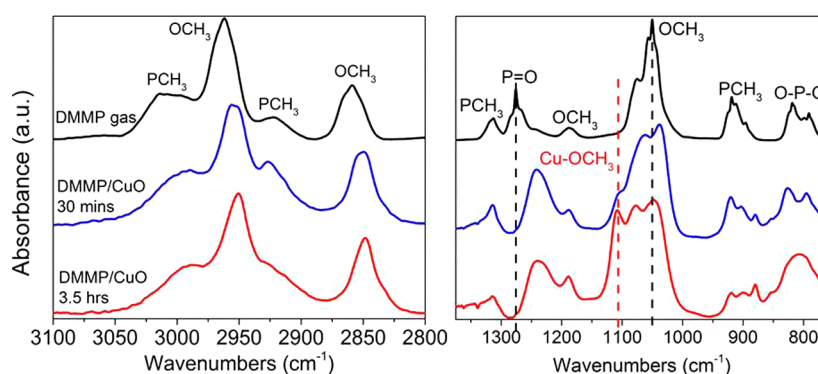
Figure 2. DRIFTS spectra of DMMP adsorbed on CuO nanoparticles at 3.5 h (bottom, red) and 30 min of exposure (middle, blue) compared to the gas phase DMMP (top, black) FTIR spectrum.

DMMP in the APXPS measurements above 1×10^{-4} Torr.[17] DMMP is also extremely persistent in the experimental endstation, and for DMMP pressures in the mTorr range and above, extensive cleaning of the sample holder and analysis chamber is required to return to UHV conditions between measurements on different samples. To avoid complicating interpretation of the surface spectra with peaks from the gas phase and to minimize contamination of the experimental endstation with DMMP, the highest dosing pressure of DMMP during APXPS is 1×10^{-4} Torr. For clarity, we will show here in the main text only the data for the measurements at the lowest (1×10^{-7} Torr) and highest (1×10^{-4} Torr) DMMP vapor pressures (p_{DMMP}) unless otherwise indicated. Spectra for all measured DMMP pressures can be found in Figures S11−S14.

Electrons were collected at an angle of 42° from the sample normal. To minimize photon-induced changes to the sample, each spectrum was taken at a new location on the surface. We observed no evidence of photon-induced damage, neither to the CuO substrate nor to surface adsorbates, over the time scale of our measurements. NEXAFS measurements were collected by scanning the photon energy while collecting electrons at a constant kinetic energy (kinetic energy = 300 eV for O K-edge and 370 eV for Cu L-edge). For XPS measurements, the incident photon energies used for each core level were chosen to give a photoelectron kinetic energy of ∼200 eV for all elements, and thus a similar sample probing depth and analyzer transmission function. Additional information regarding details of XPS data collection and peak fitting can be found in the Supporting Information, section A1 and Tables S2−S8.

CuO samples were prepared from high purity (99.999% metals basis; Alfa Aesar) Cu metal foil (0.5 mm thick). The Cu foil was cut into pieces ∼1.5 cm in diameter and cleaned by sequential sonication in acetone, isopropanol, and ethanol (20 min each). Cleaned foil pieces were thermally oxidized in air at 450 °C for 30 min, followed by sonication in ethanol. This oxidation/sonication treatment was repeated a second time to give a flake-free surface (by eye). XPS showed a mixture of CuO and Cu$_2$O after this initial thermal treatment; to fully oxidize the surface to CuO, the sample was heated in the preparation chamber of the end station at 450 °C for at least 30 min under 1 Torr of O$_2$, cooled to ∼200 °C under 1 Torr of O$_2$, and then further cooled to room temperature under a vacuum. If necessary, a final heating treatment to approximately 250−300 °C under 1×10^{-4} Torr of O$_2$ was performed to remove adventitious carbon surface contamination (see the Supporting Information, section A2). The final oxidation state was checked using a combination of NEXAFS and XPS (see the Supporting Information, section A3). The CuO samples were cooled to room temperature (20 °C) before introducing DMMP into the APXPS chamber.

2.3. DFT Calculations. The periodic solid state calculations were performed in the GGA approximation with the Perdew−Burke−Ernzerhof (PBE)[24] functional and PAW pseudopotentials[25] as implemented in the plane wave code VASP.[25−27] Since conventional DFT functionals do not describe the strong correlation effect among the partially filled Cu 3d states in CuO, the Hubbard parameter, U, is introduced for the Cu 3d electrons to describe the on-site Coulomb

interaction, within the GGA+U method[28] The values of $U = 7$ eV and $J = 0$ eV for CuO were adopted from refs 29 and 30.

In calculations of an ideal CuO crystal, the convergence criteria for the total energy were set to 10^{-5} eV, and the maximum force acting on each atom in the periodic supercell was set not to exceed 0.02 eV Å^{-1}. The $8 \times 8 \times 8$ Monkhorst−Pack k-point mesh with a kinetic energy cutoff of 450 eV was used.

The lowest energy CuO(111) surface[30,31] (Figure S6) was chosen for modeling adsorption and decomposition of DMMP. The surface slab was cut out of the relaxed CuO bulk and consisted of four atomic layers with the supercell lattice vectors of $a = 17.389$ Å, $b = 18.520$ Å, $c = 27.825$ Å, $\alpha = \beta = 90°$, and $\gamma = 102.5°$. A vacuum layer of 20 Å placed on top of the CuO(111) surface served to minimize interactions between the supercells in the c-direction and to avoid any significant overlap between wave functions of periodically translated cells.

In modeling adsorption and decomposition of DMMP on the CuO surface, the kinetic energy cutoff was set to 400 eV. The convergence criteria for the total energy was set to 10^{-5} eV, and the maximum force acting on each atom in the periodic supercell was set not to exceed 0.03 eV Å^{-1}. All surface calculations were carried out at G-point only.

Desorption energies were obtained from

$$E_{desorption} = E(CuO) + E(DMMP) - E(CuO-DMMP) \qquad (1)$$

where $E(CuO)$ is the total energy of the CuO(111) surface, $E(DMMP)$ is the total energy of the isolated DMMP molecule, and $E(CuO-DMMP)$ is the total energy of the DMMP molecule adsorbed on the CuO(111) surface.

Activation barriers and reaction kinetics, which fundamentally can be obtained, for example, by means of the nudged elastic band (NEB) method analyzing the minimum energy path for each reaction step, require forbiddingly expensive computational resources. Such a complete study of DMMP on CuO is currently beyond our capabilities. Hence, the DMMP degradation on the CuO(111) surface is discussed in section 3.3.2 in terms of feasible mechanisms and the corresponding decomposition reaction energies obtained as

$$E_{reaction} = E(C_i) - E(C_I) \qquad (2)$$

where $E(C_i)$ is the total energy of intermediate and final configurations involved in decomposition of DMMP on the CuO(111) surface and $E(C_I)$ is the total energy of the DMMP adsorbed on the CuO(111) surface corresponding to C_I, the low energy configuration (see section 3.3.2).

Bader charges were analyzed by using Bader charge analysis code.[32−34] Atomic core levels were obtained in VASP through recalculating the Kohn−Sham eigenvalues of the core states after a self-consistent calculation of the valence charge density (see ref 35).

3. RESULTS

3.1. FTIR Spectroscopy. The DRIFTS spectra for DMMP adsorbed on CuO nanoparticles after 30 min and 3.5 h of exposure are shown in Figure 2 and compared with the FTIR
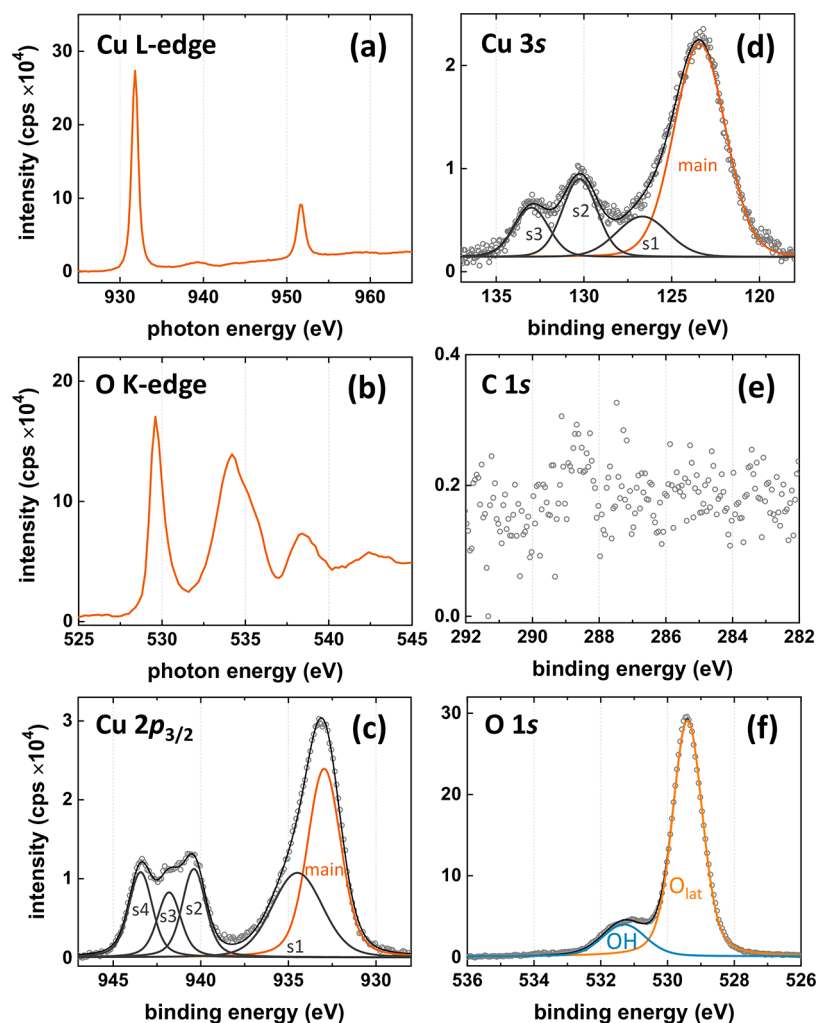
Figure 3. NEXAFS and XPS spectra of the clean CuO surface. (a) Cu *L*-edge and (b) O *K*-edge NEXAFS spectra indicate only Cu^{2+} is present. (c) Cu $2p_{3/2}$ and (d) Cu 3s XPS spectra, showing the fits for the main peak (darker) and satellite features (lighter). (e) The C 1s XPS region shows that the prepared CuO surface is free of adventitious carbon contamination. (f) The O 1s spectrum contains two peaks for the CuO lattice oxygen atoms and surface hydroxyl groups (approximately 20% OH surface coverage).

spectrum of gas phase DMMP. Gas phase DMMP vibrational frequencies and modes are in good agreement with previous data obtained by Rusu and Yates.[36] The DRIFTS spectra show that DMMP readily adsorbs and decomposes on CuO nanoparticles, indicated by the peak at 1108 cm^{-1} that corresponds to a surface methoxy group, here denoted Cu—OCH$_3$. This identification is based on prior work that investigated methanol adsorption on ThO$_2$ and CeO$_2$.[37,38] Rusu and Yates have also observed this methoxy species when DMMP adsorbs on TiO$_2$ at temperatures ranging from 79 to 213 °C.[36] Our theoretical calculations have also identified this Cu—OCH$_3$ vibration as a rocking methoxy mode δ(C—O), as described in more detail below. There may also be other surface methoxy species present, based on the increased width of the νOCH$_3$ band at 1038 cm^{-1} compared to the width of the νOCH$_3$ band in the DMMP gas phase spectrum. These results, which indicate significant formation of surface methoxy groups, agree well both with previous studies[15,36–40] as well as with our calculations (shown below) describing the vibrations of different surface methoxy species on CuO. In addition, the peak corresponding to the P=O bond of adsorbed DMMP is shifted to a lower frequency with respect to the gas phase spectrum of DMMP (1276 to 1242 cm^{-1}), which is a common feature for adsorbed DMMP on metal oxides.[36,41] This

lower frequency shift of the P=O is most likely due to a strong interaction of P=O with a metal Lewis acid site or surface hydroxyl and slightly overlaps with the δOCH$_3$ rocking vibration at 1188 cm^{-1},[36,41–45] which is also depicted in our theoretical calculations. Further interpretation of the DRIFTS spectra shows that the P—CH$_3$ peaks in both the low and high frequency regions decrease in intensity with longer exposure time, which suggests that some of the P—CH$_3$ bonds are being broken. The O—P—O peaks of DMMP at 808 cm^{-1} also appear to merge into one peak after an exposure time of 3.5 h. We speculate that this may be from formation of O$_{lat}$—P bonds when comparing our results to previous data obtained by Mitchell et al. for DMMP adsorbed on lanthana at elevated temperatures under a vacuum.[42] Although Mitchell et al. do not directly assign this peak at 808 cm^{-1}, they observe it at approximately 100 °C, which is the temperature at which they identified methyl methylphosphonate formation by integrating the methoxy peak areas in the methyl stretching region.[42]

Transmission FTIR spectroscopy was also used to investigate the formation of gas phase decomposition products in the headspace after DMMP interacts with the CuO nanoparticles (see Figure S15). After sampling the headspace of DMMP and CuO nanopowder, it was found that no new peaks were
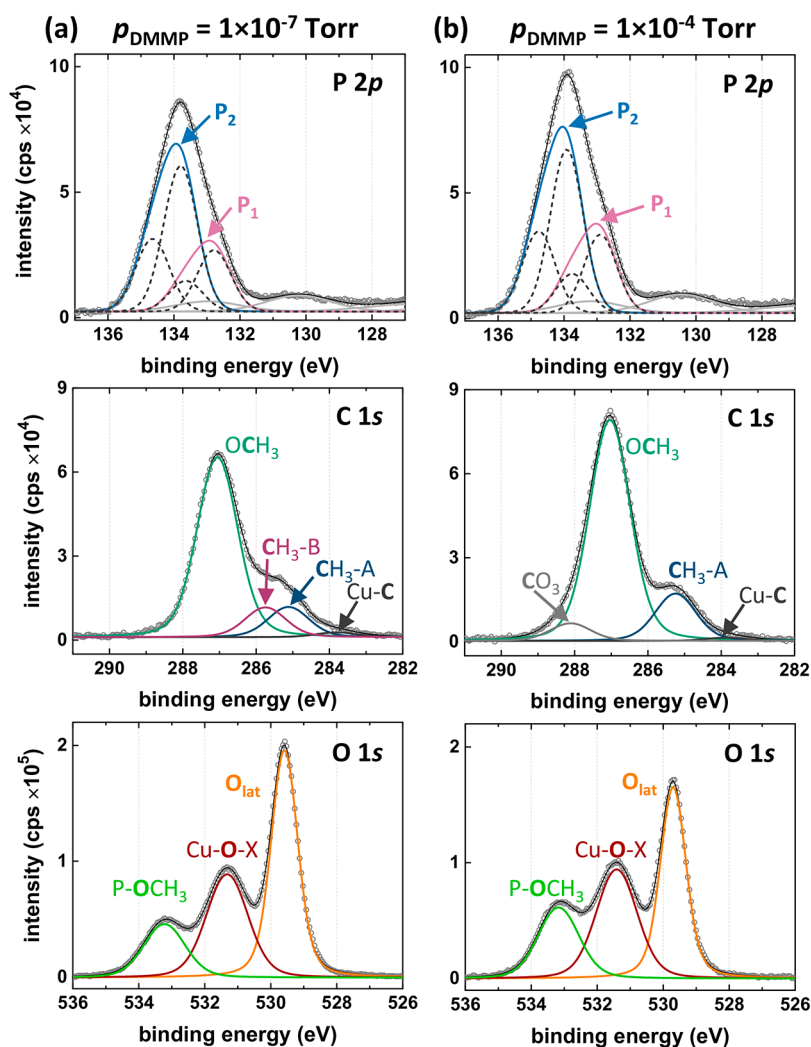
Figure 4. APXPS spectra of the CuO surface exposed to (a) 1×10^{-7} Torr and (b) 1×10^{-4} Torr of DMMP. P 2p spectra (top) have the individual spin−orbit components shown as dashed lines, and the Cu 3s satellite peaks are shown in light gray. Note the differences in scale on the vertical axis compared to Figure 3. For the same peak at the two different pressures, species labels are placed at the same position on the vertical axis as a guide for the eye.

observed, indicating that most of the DMMP decomposition products remain bound to the CuO surface.

3.2. APXPS and NEXAFS. *3.2.1. Characterization of the Clean CuO Surface.* The oxidation state of the clean oxide surface in UHV was determined using both XPS and NEXAFS (Figure 3). The Cu *L*-edge (Figure 3a) and O *K*-edge (Figure 3b) NEXAFS spectra show strong peaks near 931.8 and 529.6 eV, respectively. The overall appearance of these spectra agrees with previous measurements.[46] Notably, the main peaks expected for Cu$_2$O near 933.7 and 532.5 eV are absent,[46] indicating that the sample contains only copper oxide in the Cu^{2+} oxidation state. The Cu 2p$_{3/2}$ XPS region (Figure 3c) shows a broad main peak, with maximum intensity near 933.0 eV, that also contains a satellite feature (s1) near +1.5 eV of the main excitation peak. Other prominent satellite features (s2−s4) are observed at binding energies +7.4, +8.8, and +10.4 eV from the main peak, consistent with previous measurements.[47] The 2p satellite structure in Cu^{2+} compounds is due to multiplet splitting, arising from the interaction between the 2p core hole and 3d^9 ground configuration of the final state.[48,49]

We also collected high-resolution spectra of the Cu 3s region (Figure 3d), as some of the satellites are coincident with the binding energy region of P 2p surface species. We fit the Cu 3s

spectrum with four peaks, with the main peak at 123.4 eV, in good agreement with literature values for CuO.[50,51] The Cu 3s satellites in Cu^{2+} compounds arise from exchange splitting due to interaction between the 3d and 3s electrons in the ground state, as well as charge-transfer screening of the final-state configurations.[48,49] We fit three satellite peaks (s1−s3) at +3.3, +6.8, and +9.6 eV of the main peak. These fitting parameters are used for separating the Cu 3s satellites from surface P species after dosing with DMMP; Cu 3s fit parameters can be found in Table S2. The C 1s spectrum is shown in Figure 3e. The absence of any signal above the background indicates that the prepared sample surface is free of any adventitious carbon contamination. In the O 1s spectrum (Figure 3f), two peaks are observed at 529.4 and 531.2 eV. The peak at lower binding energy corresponds to oxygen atoms in the CuO lattice (O$_{lat}$). Since there is no adventitious carbon contamination, we assign the O 1s peak at higher binding energy to surface hydroxyl groups.[47,52] Using the method outlined in Newberg et al.,[53] we estimate an approximate 20% coverage of the surface by hydroxyl groups (see Supporting Information section S5).

3.2.2. Exposing CuO to DMMP. DMMP was introduced into the sample analysis chamber using a high precision leak valve. The P 2p spectra (Figure 4) are fit well with two doublets,

Table 1. Fitted XPS Peak Positions of the Clean CuO Surface and Relative Changes during DMMP Exposure

pressure (Torr)	Cu 2p$_{3/2}$ main peak		satellite 1 (s1)		satellite 2 (s2)		satellite 3 (s3)		satellite 4 (s4)		O 1s O$_{lat}$	
	eV (fit)	Δ[a]	eV (fit)	Δ[b]	eV (fit)	Δ[b]	eV (fit)	Δ[b]	eV (fit)	Δ[b]	eV (fit)	Δ[a]
5 × 10^{-9} (clean)	932.96		+1.53		+7.43		+8.85		+10.48		529.40	
1 × 10^{-7}	932.90	−0.06	+1.41	−0.12	+7.70	**+0.27**	+9.11	**+0.26**	+10.75	**+0.27**	529.59	**+0.19**
1 × 10^{-6}	932.92	−0.04	+1.42	−0.11	+7.76	**+0.33**	+9.15	**+0.30**	+10.79	**+0.31**	529.66	**+0.26**
1 × 10^{-5}	932.91	−0.05	+1.38	−0.15	+7.85	**+0.42**	+9.30	**+0.45**	+10.85	**+0.37**	529.69	**+0.28**
1 × 10^{-4}	932.81	−0.15	+1.48	−0.05	+7.94	**+0.51**	+9.37	**+0.52**	+10.97	**+0.49**	529.70	**+0.30**

[a]Δ is given relative to the position of the clean measurement. [b]Δ is given relative to the Cu 2p$_{3/2}$ main peak for each pressure condition.

indicating phosphorus atoms in two distinct chemical environments (labeled P$_1$ and P$_2$), with P 2p$_{3/2}$ peaks at 132.8 and 133.8 eV. (The spin−orbit components of the P 2p doublets are shown in Figure 4 as dashed lines.) The remaining features in the P 2p spectra correspond to the Cu 3s satellite structures. The observation of more than one P-containing species is a clear indication that DMMP is decomposing at room temperature.

The C 1s spectra show significant changes as the DMMP pressure is increased. At $p_{DMMP} = 1 \times 10^{-7}$ Torr, three peaks dominate at 285.1, 285.8, and 287.1 eV. With increasing DMMP pressure, the peaks at 285.1 and 287.1 eV increase in intensity, while the peak at 285.8 eV decreases significantly and disappears at $p_{DMMP} = 1 \times 10^{-4}$ Torr (the position of this peak was fixed during fitting for $p_{DMMP} \geq 1 \times 10^{-6}$ Torr). Additionally, a much smaller peak is observed near 283.8 eV. This peak is not at a binding energy typical for adventitious carbon contamination, and thus is likely due to a DMMP decomposition product; the low binding energy suggests the formation of a Cu−C bond. Since the area of this peak is so small and remains essentially constant at all DMMP vapor pressures, we do not consider its formation to be a dominating chemical process, and we will not comment on it further here. Finally, for $p_{DMMP} \geq 1 \times 10^{-5}$ Torr, another small peak is observed at 288.1 eV. At increasing DMMP pressures, adventitious carbon contamination on the chamber walls can be displaced by DMMP molecules and may subsequently adsorb on the sample surface. This peak is in the region where we typically see adventitious carbon contamination on CuO surfaces (see Figure S2), and the size of this peak was larger for experiments where the background chamber pressure was higher. Thus, we identify this as surface carbonate contamination, which is taken into consideration during quantitative analysis of the O 1s spectra.

The O 1s spectra contain three main features. In addition to the CuO lattice oxygen (O$_{lat}$) peak at low binding energy, a peak at 533.2 eV is observed which we attribute to methoxy species bound to phosphorus (P−OCH$_3$). The intermediate binding energy region contains a small contribution from surface carbonate species (only at $p_{DMMP} \geq 1 \times 10^{-5}$ Torr, see Figure S2) but is otherwise primarily due to contributions from moieties which we label as "Cu−O−X" type. These include coordination of phosphoryl groups to the oxide surface through Cu−O−P moieties and methoxy groups bound directly to the metal oxide surface[15] (Cu−O−CH$_3$). While the P−OCH$_3$ and O$_{lat}$ oxide peaks are well resolved, fitting individual peaks for different Cu−O−X groups would require more information on the chemical mechanism. At this point in the analysis, we fit this region with only one peak which contains contributions from all Cu−O−X and carbonate species. During quantitative analysis of the XPS data, we calculated the contribution from carbonate species using C/O relative sensitivity factors measured from gas phase CO$_2$ (see the Supporting Information, section A2). The remaining peak intensity is then assigned to Cu−O−X groups.

Changes in the Cu 2p$_{3/2}$ satellites, O 1s binding energy, and valence band spectra for CuO were observed upon DMMP decomposition. The position of the O 1s peak for O$_{lat}$ is shifted to higher BE by approximately +0.3 eV upon exposure of the sample to 1×10^{-7} Torr DMMP, while the Cu 2p$_{3/2}$ peak position remains unchanged. This shift in the O$_{lat}$ O 1s peak was found to be reproducible across multiple measurements on different samples and is thus not simply an artifact of charging or changes in the nominal photon energy. We also observed decreases in intensity and shifts to higher binding energy of the well-separated Cu 2p$_{3/2}$ satellite structures at +7.4, +8.8, and +10.4 eV from the main peak with increasing DMMP pressure (see Figure S11). Table 1 shows the fitted positions of the Cu 2p$_{3/2}$ and O 1s peaks for CuO at all pressures, as well as the Cu 2p$_{3/2}$ satellite peak positions relative to the main peak. The difference in the peak positions for the Cu 2p$_{3/2}$ main peak and O 1s peak is given relative to the peak position of the clean surface, while the difference in peak positions for the Cu 2p$_{3/2}$ satellites is given relative to the Cu 2p$_{3/2}$ main peak. The small value of Δ for the Cu 2p$_{3/2}$ main peak and s1 likely results from an error in the peak fitting procedure, since these two fitted peaks overlap significantly. However, the Cu 2p$_{3/2}$ satellites (s2−s4) are well resolved from the main peak and from each other, and the magnitude of Δ for s2−s4 correlates with the magnitude of Δ for the CuO O 1s peak.

The valence band XPS spectra for each p_{DMMP} are shown in Figure 5, and there are three regions highlighted in the figure. Region **1** is dominated by the O 2p and Cu 3d^9 L^{-1} states (where L^{-1} indicates the ligand hole after charge transfer of an electron from a 2p ligand (oxygen) level to a metal 3d level), region **2** contains features primarily from the Cu 3d^8 valence configuration, and region **3** shows the O 2s peak and a feature from the Cu 3d^8 configuration.[48,51,52,54−56] Comparison to a valence band spectrum collected for a pure Cu$^+$ oxide (Cu$_2$O, see Figure S16) supports our hypothesis that the changes observed with DMMP dosing are likely not due to a change in the oxidation state of a significant portion of the surface Cu atoms. We also see no indication that the Cu oxidation state is changing in the NEXAFS Cu L-edge spectrum after DMMP exposure (see Figure S4); thus, we attribute the changes in the valence band and Cu 2p$_{3/2}$ satellite structures to the presence of surface adsorbates rather than to changes in Cu oxidation state.

3.3. DFT Modeling. The optimized lattice constants of the monoclinic CuO unit cell with the C2/c space group (Figure 6a) were $a = 4.657$ Å, $b = 3.452$ Å, and $c = 5.118$ Å, which is in agreement with experimentally determined values[57,58] within 1%. Figure 6a shows the bulk structure and antiferromagnetic spin ordering in bulk CuO. The calculated local magnetic moment per Cu atom (0.67 μ_B) is consistent with experiment (0.69 μ_B)[59] and earlier DFT+U estimations (0.63 and 0.68 μ_B).[31,30] The PBE+U-calculated band gap is 1.6 eV, which is in better agreement with the experimentally measured value (~1.9 eV)[60] than previous
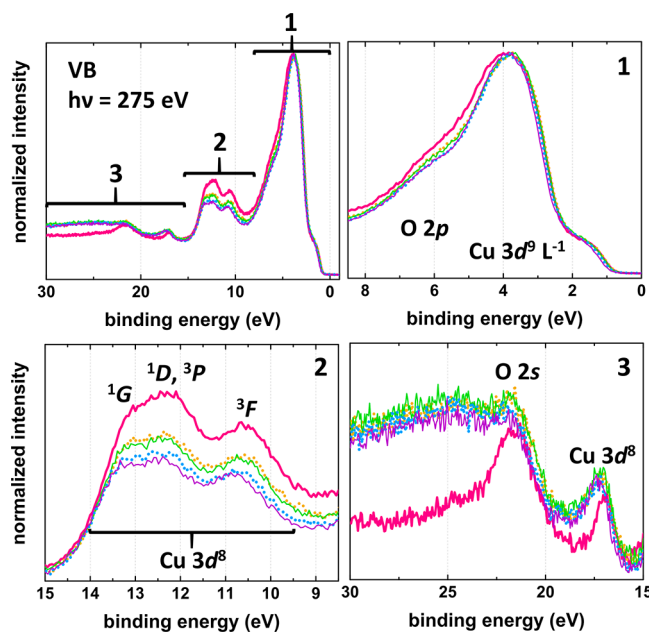
Figure 5. Valence band XPS spectra as a function of increasing DMMP pressure (pink, thick line = clean surface; orange dots = 1×10^{-7} Torr DMMP; green line = 1×10^{-6} Torr DMMP; blue dots = 1×10^{-5} Torr DMMP; purple line = 1×10^{-4} Torr DMMP). Excitation energy $h\nu$ = 275 eV.
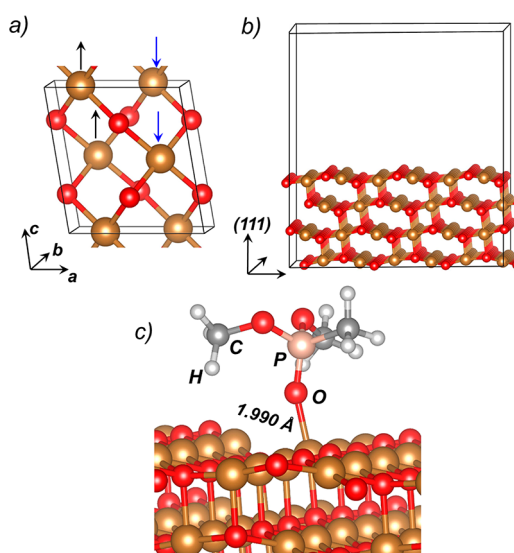
Figure 6. (a) Monoclinic unit cell of CuO(black and blue arrows demonstrate the direction of the local magnetic moment). (b) Side view of the pristine CuO(111) surface. (c) Side view of DMMP adsorbed on the CuO(111) surface.

DFT+U estimations (1.1 and 1.3 eV).[30,31] The top of the conduction band is formed by Cu 3d and O 2p states, while the bottom of the conduction band is predominantly formed by Cu 3d states (see Supporting Information section A6 for more details). The lowest energy CuO(111) surface[30,31] (Figure 6b) was chosen for modeling adsorption and decomposition of DMMP.

3.3.1. DMMP Adsorption. Experimental and theoretical studies of DMMP adsorption on different metal oxides suggest that the molecule typically interacts with one of the surface metal atoms through its phosphoryl oxygen.[15,36,61] Our simulations

show that DMMP indeed tends to adsorb on the CuO(111) surface by forming a bond between the phosphoryl oxygen and an under-coordinated surface Cu atom (Figure 6c). The calculated desorption energy is 66.2 kJ mol^{-1}. Inspection of the change in local atomic charge density obtained through a Bader analysis does not reveal any noticeable charge redistribution between the molecule and the surface. The calculated Bader charge localized on the adsorbed DMMP molecule is only +0.07 e.

Oxygen vacancies are common defects on metal oxide surfaces and have been shown to play an important role for molecular adsorption and the chemical stability of the adsorbed molecule,[62−64] including the specific case of DMMP adsorption on MoO$_3$.[17] Oxygen vacancies introduced on the CuO(111) surface, however, do not have a strong effect on DMMP adsorption due to a rearrangement of adjacent-to-vacancy Cu atoms (see Supporting Information section A7). The calculated desorption energy of DMMP on the CuO surface containing oxygen vacancies is 70.8 kJ mol^{-1}, which is only 4.2 kJ mol^{-1} higher than the desorption energy obtained for the pristine surface. Because the oxygen vacancy seemed to barely affect adsorption of DMMP on CuO(111), all further simulations of decomposition reaction mechanisms were carried out for the pristine CuO(111) surface only.

3.3.2. DMMP Decomposition. In studying DMMP decomposition on the CuO(111) surface, we modeled several possible reaction pathways (Figure 7). The primary C_1−C_2 step, which is common for all mechanisms, proceeds through a rotation of the P−OCH$_3$ moiety about the −OCH$_3$ bond. One of the possible decomposition pathways is associated with the breaking of an O−CH$_3$ bond in configuration C_2 and the subsequent formation of a surface Cu−CH$_3$ group (path C_1−C_2−C_3). The calculated reaction energy of this channel is 91.9 kJ mol^{-1} (endergonic). In contrast, the formation of an O$_{lat}$−CH$_3$ surface methoxy group (path C_1−C_2−C_4) is a thermodynamically favorable (exergonic) process and proceeds with an energy release of 72.0 kJ mol^{-1}.

Further, we simulated two reaction channels for O$_{lat}$−CH$_3$ formation through a cleavage of the P−CH$_3$ bond (paths C_1−C_6 and C_1−C_7). Both of these channels have the common steps C_2−C_5, proceeding through the cleavage of a P−OCH$_3$ bond in the intermediate structure C_2. As a result, one surface Cu—OCH$_3$ methoxy group is formed and the phosphorus atom of the molecular residue forms a new bond with a surface oxygen (P−O$_{lat}$). The reaction steps C_5−C_6 and C_5−C_7 are associated with the formation of an additional O$_{lat}$−CH$_3$ surface methoxy group through P−CH$_3$ bond breaking and the formation of another P−O$_{lat}$ bond. The decomposition channel C_1−C_6 is the most thermodynamically favorable path, with a calculated exothermicity of −75.1 kJ mol^{-1}.

3.3.3. Core Level Ionization Energies. To compare results of XPS measurements and DFT calculations, C 1s, O 1s, and P 2p core level ionization energies were calculated for intact DMMP molecules adsorbed on the pristine CuO(111) surface (C_1), as well as for products and intermediate structures of the proposed decomposition pathways shown in Figure 7. These results are collected in Table 2 and reveal a strong negative shift (∼2 eV) of the 1s level of the O2 oxygen atom for configurations C_4−C_7. This shift is associated with the formation of the surface Cu−OCH$_3$ methoxy groups. Cleavage of the P−CH$_3$ bond in configuration C_5 and the subsequent formation of a surface O$_{lat}$−CH$_3$ methoxy group (configurations C_6 and C_7) is accompanied by a positive shift (1.0 and 0.85 eV, respectively) of the 1s level of the C1 atom. These calculations are in good agreement with
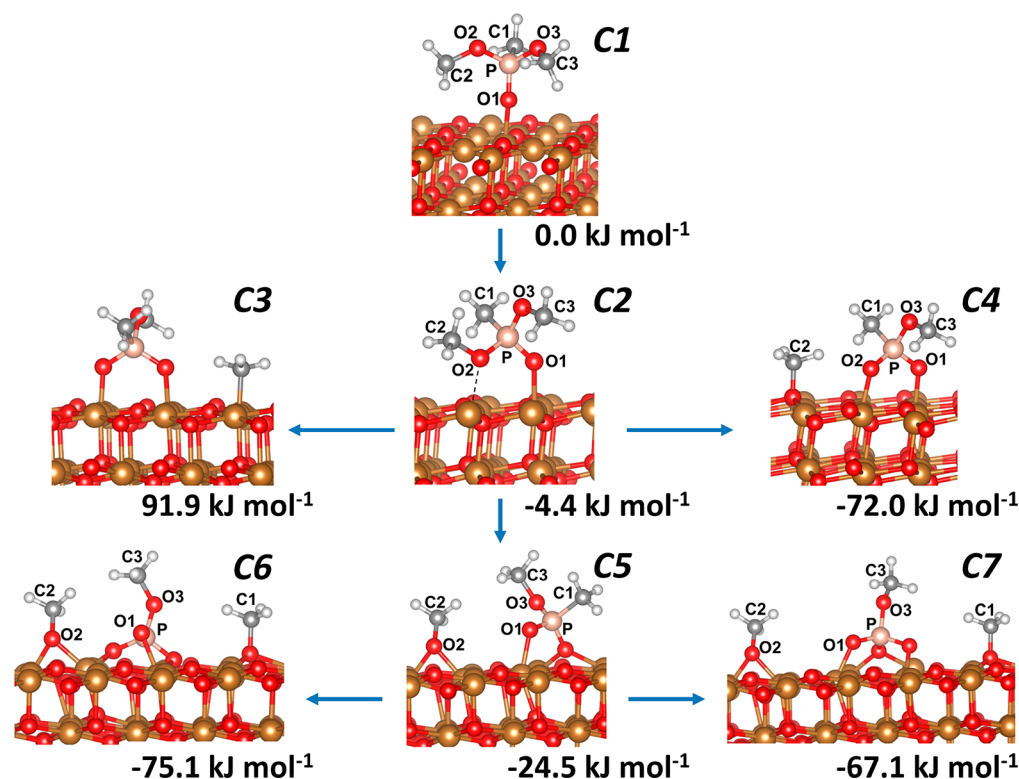
Figure 7. Scheme of DMMP decomposition on the CuO(111) surface.

Table 2. Relative to Configuration C_1 Shifts in Calculated O 1s, C 1s, and P 2p Core Level Ionization Energies

atom	core level	bond	configuration					
			C_1	C_2	C_4	C_5	C_6	C_7
O1	1s	P=O	0.0	0.23	−0.90	−0.01	−0.16	−0.31
O2	1s	O—C	0.0	0.73	**−2.13**	**−1.96**	**−1.92**	**−1.98**
O3	1s	O—C	0.0	0.34	−1.02	−0.08	−0.24	−0.48
P	2p		0.0	0.33	−1.21	−0.13	−0.14	−0.19
C1	1s	P—C	0.0	0.31	**−0.85**	0.03	**1.00**	**0.85**
C2	1s	O—C	0.0	0.39	−0.36	−1.38	−1.36	−1.52
C3	1s	O—C	0.0	0.26	−0.69	0.17	−0.05	−0.20

Table 3. Calculated and Experimental Vibrational Frequencies (in cm^{-1}) of Isolated and Adsorbed DMMP Molecule and Methoxy Moieties

	gas phase			adsorbed on CuO surface					
								Cu—OCH$_3$	
	DMMP		•OCH$_3$	DMMP		Cu—OCH$_3$	O$_{lat}$—CH$_3$	atop	bridge
vibrational mode	Exp.	DFT^a		Exp.	DFT	Exp.		DFT^b	
ν(P=O)	1276	1211	n/a	1242 (−34)^c	1162 (−49)	n/a	n/a	n/a	n/a
δ(O—CH$_3$)	1188	1177	898	1188	1180	1108	1151	1115	1088
ν(C—O) (a)	1076	1092	1102	1062 (−14)	1090 (−2)		995	1050	955
ν(C—O) (s)	1050	1064		1038 (−12)	1053 (−11)				

^{a}Vibrational frequencies calculated using the PBE functional. ^{b}All surface calculations were carried out using the PBE+U functional. ^{c}Shifts relative to the gas phase are given in parentheses.

experimental values measured by XPS, as will be detailed in the Discussion section.

Decomposition of DMMP on the CuO(111) surface through reaction paths C_1–C_6 and C_1–C_7 leads to a significant rearrangement of surface atoms. The largest displacements of surface atoms were observed for configurations C_5, C_6, and C_7 where the phosphorus atom of DMMP forms new bonds with either one or two surface oxygen atoms (bond lengths and atomic displacements are tabulated in the Supporting Information, Tables S9 and S10). Such changes in geometry parameters should, in turn, lead to shifts in core levels of surface atoms. Indeed, the calculated O 1s core levels for O$_{lat}$ atoms that form new bonds with DMMP decomposition products are shifted to higher energies by ~1.5−2 eV (see Table S12). We also

calculated ionization energies for Cu 2p and Cu 3s core levels, which are collected in Table S11. However, the DFT calculations do not show changes in the electronic structure of the CuO substrate. (See Supporting Information section A8 for more details.)

3.3.4. Vibrational Frequencies. We calculated vibrational frequencies for a gas phase DMMP molecule, the DMMP molecule adsorbed on the CuO(111) surface (C_1, Figure 7), and the various surface methoxy species formed during DMMP degradation (O_{lat}−CH$_3$ and Cu−OCH$_3$ in C_4−C_7, Figure 7). Gas phase DMMP was simulated in VASP by placing an isolated molecule into a large box with lattice parameters a = 17.389 Å, b = 18.520 Å, c = 27.825 Å, $\alpha = \beta$ = 90°, and γ = 102.5°, similar to those of the surface supercell used for modeling adsorption and decomposition of DMMP (Figure 6b).

Table 3 shows that the PBE functional tends to underestimate slightly the ν(P=O) frequency relative to the experimentally determined values. DFT identifies three distinct groups of vibrations in the region 1250−1000 cm^{-1}: ν(P=O) at 1211 cm^{-1}, δ(O−CH$_3$) at ~1177 cm^{-1}, and ν(C−O) at 1092 and 1064 cm^{-1}, all of which are in good qualitative agreement with our experiments (Figure 2) and earlier calculations.[61]

The calculated ν(P=O) frequency of DMMP adsorbed on the CuO(111) surface shifts lower by ~50 cm^{-1} relative to the gas phase molecule. The position of the δ(O−CH$_3$) mode is only slightly affected (by ≤3 cm^{-1}) by interactions with the surface. This is consistent with our FTIR measurements, which show that the positions of ν(P=O) and δ(O−CH$_3$) bands are closer to each other when DMMP interacts with the CuO surface (Figure 2), and is also in good agreement with results of recent DFT simulations of DMMP adsorbed on γ-Al$_2$O$_3$[61] and metal−organic frameworks.[10] The calculated positions of ν(C−O) modes are red-shifted (2−11 cm^{-1}) relative to gas phase DMMP, which agrees well with our experiments (12−14 cm^{-1}) described above.

Next, we calculated vibrational frequencies for different configurations of the surface methoxy species (Figure 8).

Cu-OCH$_3$ (atop)   Cu-OCH$_3$ (bridge)   O$_{lat}$-CH$_3$
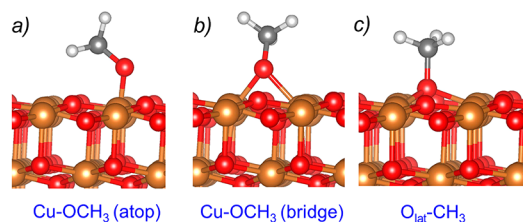
Figure 8. (a) Atop and (b) bridge adsorption configurations of methoxy on the CuO(111) surface. (c) O$_{lat}$−CH$_3$ surface methoxy configuration.

These configurations correspond to DMMP degradation products Cu−OCH$_3$ and O$_{lat}$−CH$_3$ on the CuO(111) surface for C_4−C_7 (Figure 7), rather than methoxy groups bound to a P atom. To aide in interpretation of frequency shifts calculated for the surface methoxy groups shown in Figure 8, vibrations for a methoxy radical species in the gas phase were also calculated. Frequencies of ν(C−O) and δ(O−CH$_3$) modes in an isolated ●OCH$_3$ moiety, −OCH$_3$ fragments of gas phase DMMP, and surface Cu−OCH$_3$ and O$_{lat}$−CH$_3$ groups were then compared. The calculated frequency of the ν(C−O) mode in ●OCH$_3$ is 1102 cm^{-1}, which agrees well with the position of the band at 1108 cm^{-1} (Figure 2) observed only after exposing CuO nanoparticles to DMMP. The calculated positions of the ν(C−O) modes in atop (1050 cm^{-1}) and bridging (955 cm^{-1}) Cu−

OCH$_3$ as well as O$_{lat}$−CH$_3$ (995 cm^{-1}) are shifted to much lower frequencies compared to the gas phase ●OCH$_3$ radical (1102 cm^{-1}). Such strong shifts in the positions of ν(C−O) modes can be explained by noticeable differences in the O−CH$_3$ bond distances. The calculated O−CH$_3$ bond distance in ●OCH$_3$ is 1.358 Å, whereas the O−CH$_3$ bond is longer by ~0.05−0.1 Å in the surface-bound methoxy species (CuO−CH$_3$ atop = 1.401 Å, CuO−CH$_3$ bridging = 1.417 Å, O$_{lat}$−CH$_3$ = 1.452 Å).

Calculated positions of δ(O−CH$_3$) modes in the atop (1115 cm^{-1}) and bridging (1088 cm^{-1}) methoxy configurations are consistent with the experimentally observed band at 1108 cm^{-1}. Similar trends were reported for methoxy groups on polycrystalline ceria with IR bands observed at 1108 and 1065 cm^{-1} assigned to ν(C−O) stretching modes in atop and doubly bridging (respectively) surface methoxy species.[37] The calculated frequency of the δ(O−CH$_3$) mode for the O$_{lat}$−CH$_3$ configuration is 1151 cm^{-1}. This value is also consistent with the broad νOCH$_3$ region observed in Figure 2.

The data collected in Table 3 demonstrate the overall good agreement between the experimentally measured and calculated frequencies of vibrations for both gas phase DMMP and DMMP adsorbed on the CuO surface. The combination of experiment and theory allows for assignment of distinct vibrational modes near ~1100 cm^{-1} corresponding to the formation of different surface methoxy groups.

4. DISCUSSION

The combined analysis of DRIFTS, DFT, and XPS gives us unique insight into the mechanism of DMMP decomposition on the CuO surface that cannot be obtained by any one of these methods alone. Our data are most consistent with the DMMP decomposition proceeding through room-temperature breaking of P−CH$_3$, P−OCH$_3$, and PO−CH$_3$ bonds, with subsequent formation of O$_{lat}$−CH$_3$, O$_{lat}$−P, and Cu−OCH$_3$ groups, as shown in C_4−C_7 of Figure 7. Understanding the details of the formation of surface methoxy groups and the associated changes in the electronic structure of the CuO substrate upon exposure to DMMP is paramount to building a comprehensive picture of the DMMP decomposition mechanism, and we will address these two points separately. The role of surface hydroxyl groups in this mechanism is unclear, and we will also discuss this in detail below. Finally, we will show that quantitative analysis of the APXPS data gives excellent agreement with the proposed mechanism.

4.1. Mechanism of Formation of Surface Methoxy Groups. Our DFT calculations show several possible pathways by which the interactions between DMMP and CuO can lead to the formation of surface methoxy groups. The reaction pathway C_1−C_2−C_4 (see Figure 7) involves breaking of a PO−CH$_3$ bond and the subsequent formation of a PO−Cu bond and an O$_{lat}$−CH$_3$ bond. This pathway gives no net change in the relative number of OCH$_3$ groups, and the remaining DMMP fragment in configuration C_4 lies in an energetic sink after this step. In contrast, the reaction pathway C_1−C_2−C_5 can produce one additional net surface methoxy group by the formation of C_6 or C_7 following P−CH$_3$ bond scission. Removal of the first P−OCH$_3$ also results in a decreased calculated ionization energy for the C1 atom in configurations C_4 and C_5 relative to C_1 and C_2 (see Table 2). This decreased ionization energy is observed in XPS as a shift of the methyl group to lower binding energy by ~0.7 eV (CH$_3$-A). The shift to lower binding energy indicates a weakening of the P−CH$_3$ bond.

Our corroborating DRIFTS and DFT results show that the phosphoryl group is strongly coordinated to the CuO surface, which is consistent with the general mechanism of DMMP adsorption on metal oxide surfaces.[1,15,17−19,41,42,65] We also observe changes in the vibrations associated with P−OCH$_3$, P−CH$_3$, and O−P−O moieties, which are rarely seen at room temperature. The formation of surface methoxy moieties Cu−OCH$_3$ appears in DRIFTS as a signature peak at 1108 cm^{-1}, which was not observed for gas-phase DMMP. The increase in intensity across the broad region 1000−1150 cm^{-1} suggests the formation of multiple types of surface methoxy groups. Our DFT calculations are consistent with these data and suggest both O$_{lat}$−CH$_3$ and Cu−OCH$_3$ (both bridging and atop) formation. Furthermore, decreasing P−CH$_3$ intensity and broadening of O−P−O bands are consistent with a mechanism where P−CH$_3$ bonds are breaking (C_6/C_7) and P−O$_{lat}$ bonds are forming (C_5, C_6/C_7).

The formation of surface O$_{lat}$−CH$_3$ groups via P−CH$_3$ bond breaking is further confirmed by an analysis of the relative peak-area ratios of the surface species observed by XPS. For intact adsorbed DMMP (C_1), the ratio of OCH$_3$ to CH$_3$ in the C 1s spectrum should be 2:1. However, the data show that the OCH$_3$ peak (287.0 eV) is much larger, with a ratio of the 287.0 eV peak to the sum of all other C peaks being 3:1 or greater at all DMMP pressures. Likewise, the OCH$_3$ and Cu−O−P groups should appear also in a 2:1 ratio for intact DMMP, but the OCH$_3$/Cu−O−X peak area ratio is always between 1:2 and 1.3:2. These data show that excess OCH$_3$ groups are present on the CuO surface relative to what is expected for intact DMMP adsorption and are thus indicative of DMMP decomposition.

Removal of a P−OCH$_3$ group has been observed on many other metal oxides at or near room temperature.[1,15,65] However, CuO provides a rare example of P−CH$_3$ bond breaking at room temperature.[66−68] Room-temperature PO−CH$_3$ bond breaking (to give configuration C_4) is a mechanism that, to the best of our knowledge, has not been reported previously on any metal oxide.

For many metal oxides, P−OCH$_3$ bond breaking is presumed to proceed through a hydrolysis mechanism, for which the presence of surface hydroxyl groups and/or molecular water (often at defect sites) is critical.[14,17,65,68] Gas phase species, specifically methanol, are typically observed as hydrolysis decomposition products,[17,65] and our previous study on MoO$_3$ showed that the proton in methanol formation had to come from a surface hydroxyl group.[17] No gas phase products are observed at room temperature for DMMP decomposition on CuO, either when starting from UHV (XPS) or ambient (FTIR) conditions. Furthermore, the XPS and FTIR results corroborate one another, despite the larger concentration of surface OH expected under the ambient FTIR conditions. This supports our hypothesis that the surface hydroxyl groups are likely not dominant players in the decomposition mechanism. However, we cannot completely exclude participation of the hydroxyl groups in the reaction, as their signature peak in XPS would be buried under that of the Cu−O−X species. Hence, the role of water/hydroxyl groups present on the surface of CuO in the chemistry of DMMP adsorption/decomposition has yet to be clarified.

One plausible hypothesis is that surface hydroxyl groups play a role in the formation of configuration C_5. This configuration resembles the product typically proposed after hydroxyl-mediated breaking of the P−OCH$_3$ bond, with movement of a methoxy group from the P atom to the oxide surface. This step could be mediated or catalyzed by hydroxyl groups, leaving the methoxy group protonated on the CuO surface, but with a high desorption energy at room temperature such that gas-phase methanol is not observed. Alternatively, a surface OH group could catalyze breaking of the P−OCH$_3$ bond, with subsequent migration of the proton to a nearby O$_{lat}$ site, where OH would then be available for another subsequent reaction. This type of hydroxyl surface hopping has been suggested previously for metal oxide surfaces, including Y$_2$O$_3$.[14] We are currently investigating the effect of changing relative humidity (and thus the number of surface hydroxyl groups) on DMMP decomposition on CuO and performing isotopic labeling studies to provide additional insight into these possible mechanisms.

Initial adsorption at surface hydroxyl groups and degradation by hydrolysis are also common mechanistic elements of decomposition of the live organophosphorous nerve agents.[1,69] The results presented here suggest that hydroxyl-mediated bond-breaking alone is insufficient to describe the adsorption/decomposition mechanism of DMMP on CuO. Further study of CuO with actual CWAs or other simulants containing P−F moieties is clearly required to better understand the mechanism of CWA degradation.[8] However, these experiments fall outside of our capabilities due to safety concerns. Nevertheless, the strong corroboration between our spectroscopic experiments and DFT calculations is encouraging. Meaningful DFT simulations of sarin or any other highly toxic organo-phosphonates would not be possible without the spectroscopically informed results of the current study.

4.2. Changes in the Electronic Structure. The formation of new covalent bonds involving lattice oxygen atoms has a marked effect on the XPS results and DFT calculations. The calculated core-level ionization energies indicate that the formation of new Cu−O bonds with the surface results in a significant shift (∼2 eV) of the O 1s core level to lower energies for surface-bound methoxy groups. The increase in the 531.4 eV O 1s peak intensity relative to that of the 533.2 eV peak is diagnostic of increased OCH$_3$ moieties on the CuO surface, which is consistent with the proposed mechanism.

CuO lattice oxygen atoms are known to participate in strong ligand-to-metal charge transfer, resulting in the closed-shell 3d^{10}L^{-1} valence configuration rather than the 3d^9 open-shell Cu^{2+} state. This strong ligand-to-metal charge transfer explains the shift of the O$_{lat}$ O 1s peak relative to the Cu peaks upon adsorption/decomposition of DMMP. As DMMP adsorbs and decomposes, O$_{lat}$ atoms form new covalent bonds with surface adsorbates, drawing electron density away from the CuO substrate. These (former) lattice oxygen atoms, now in a new bonding environment (Cu−O−X), show a significant shift to higher binding energy (∼2 eV). This is accompanied by a smaller shift (∼0.25 eV) of the O$_{lat}$ O 1s peak (i.e., the remaining lattice oxygen atoms that have *not* formed new bonds with surface adsorbates) as well as a shift to higher binding energy of the satellites in the Cu 2p$_{3/2}$ spectrum.

Together, these changes in the XPS spectra indicate that the electronic environment of the "bulk" lattice oxygen atoms (∼2−3 atomic layers of CuO) probed by XPS is also affected by the presence of the surface adsorbates. Since the Cu 2p$_{3/2}$ main peak and satellites arise from different electronic states (namely, the charge-transfer 3d^{10}L^{-1} and 3d^9 ground states, respectively), the distance between the main 2p$_{3/2}$ peak and the satellites is directly related to the energy required for charge transfer to occur. A shift to higher binding energy of the satellites with respect to the main peak thus indicates an increase in the charge-transfer energy. The Cu 3s core-level and valence band spectra also show no change in

the main excitation peak positions, which correspond to the charge-transfer state. These results suggest that, as the surface oxygen atoms pull electron density to the surface to form new covalent bonds, the remaining "bulk" lattice oxygen atoms continue to shield the Cu atoms through ligand-to-metal charge transfer, although at a higher energy cost. This hypothesis also offers a feasible explanation to the discrepancies in the DFT core-level ionization calculations for Cu 2p, Cu 3s, and O_{lat} 1s levels, as DFT is likely to underestimate the effects of ligand-to-metal charge transfer that results in the $d^{10}L^{-1}$ state.

4.3. Quantitative Analysis of the DMMP Decomposition Mechanism. The XPS spectra collected at different DMMP pressures were normalized (by multiplication) to a common background intensity at the low binding energy side for each set of core level spectra. This normalization allows us to directly compare spectra across a range of p_{DMMP} while accounting for differences in the signal intensity due to attenuation of XPS signal by gas-phase molecules or small changes in the aperture–sample distance when moving to a new sample spot. Background-normalized spectra for the O 1s region are shown in Figure S17. It is clear that the greatest changes occur between the spectrum of the clean surface and that of the surface exposed to $p_{DMMP} = 1 \times 10^{-7}$ Torr. With increasing DMMP pressure, the changes in the spectra become more subtle. The peak areas for methoxy (both O 1s and C 1s), the O 1s peak for Cu–O–X species, and the P_1 P 2p peak increase with increasing p_{DMMP}. The C 1s peak area for the CH_3-A methyl group increases, while the CH_3-B methyl group decreases.

Comparing the rates of attenuation of the different CuO substrate peaks supports the participation of lattice oxygen atoms in our proposed mechanism. Because we are collecting photoelectrons with similar kinetic energy for each core level, we can expect that the signals from the CuO substrate (Cu 2p, Cu 3s, and O 1s) should all attenuate at the same rate if the CuO surface atoms are not involved in DMMP decomposition. However, we see clearly in Figure 9a that the O 1s peak for O_{lat} is more attenuated than the Cu 3s and Cu $2p_{3/2}$ main peaks. This intensity change is consistent with a mechanism where the surface O_{lat} atoms form $P–O_{lat}$ bonds and $O_{lat}–CH_3$ bonds. Furthermore, DFT calculations predict a shift to higher binding energy of ~1.5–2 eV for lattice oxygen atoms that form new bonds with the surface decomposition products, which is consistent with the Cu–**O**–X O 1s peak observed at 531.4 eV. Reaction of lattice oxygen atoms during DMMP decomposition has been previously reported for many oxides, including CeO_2[15] and TiO_2;[65] however, P–CH_3 bond breaking still requires elevated temperatures in almost all cases. Limited P–CH_3 bond-breaking has been reported on TiO_2 at extended exposure times (after depletion of free surface OH groups).[45] Another exception may be Fe_2O_3, where it has been suggested that P–CH_3 bond cleavage can occur near room temperature via a Mars and van Krevelen type of mechanism.[66,67] Mitchell et al. showed that, compared to other metal oxides, P–CH_3 bond cleavage on Fe_2O_3 is facile at elevated temperatures. However, in that study, the P–CH_3 bonds appear to remain intact until 200–300 °C.[42] A quantitative XPS analysis of DMMP decomposition over Fe_2O_3 would help to clarify this point.

The rates of attenuation for the CuO O 1s peak and the Cu $2p_{3/2}$ satellites (s2–s4) are almost identical. As discussed in the previous section, both of these spectral features are shifted to higher binding energy due to an increased charge-transfer energy between lattice O and Cu atoms upon incorporation of lattice oxygen atoms into the decomposition products. The area under
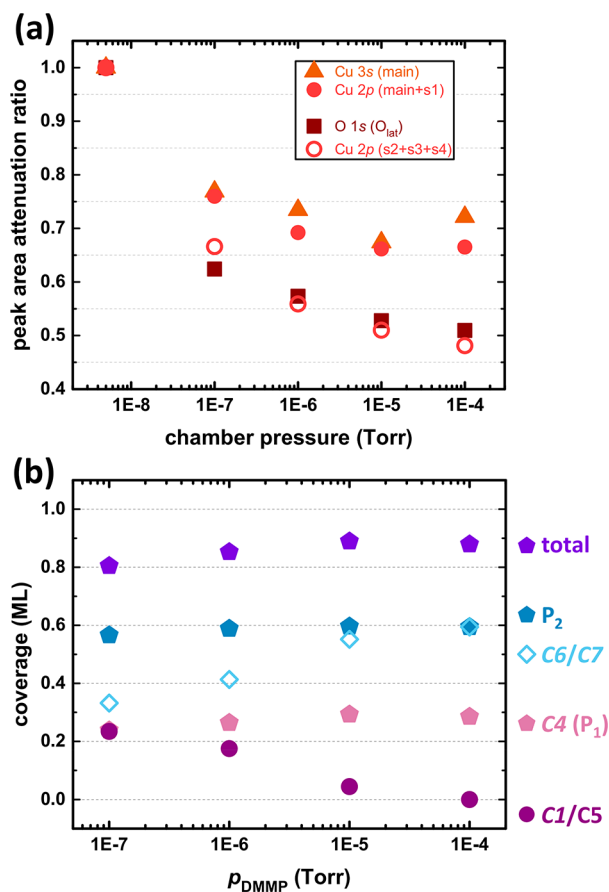
Figure 9. (a) Attenuation rates of XPS peaks corresponding to atoms in the CuO lattice. (b) Coverage calculations of different DMMP decomposition species. Pentagons indicate values calculated from P 2p peak areas, circles indicate values calculated using the CH_3-A/CH_3-B ratio, and diamonds indicate values calculated from the P_2 difference area (total P_2 area) − (calculated P_2 fraction of C_1/C_5).

the O_{lat} O 1s peak decreases due to two factors: (1) conversion of O_{lat} atoms into Cu–O–X moieties and (2) attenuation of the total O_{lat} intensity as surface adsorbates accumulate. The Cu $2p_{3/2}$ satellite structures result from interactions between the lattice O 2p and Cu 3d orbitals, and thus, the number of these interactions should decrease stoichiometrically as the number of O_{lat} atoms decreases. The Cu 3s satellites also appear to shift somewhat to higher binding energies, but quantification and confirmation of this effect is further complicated by the overlapping P 2p peaks once the surface is exposed to DMMP.

The binding energies in Table 2 predicted by DFT are used to help in assignment of peaks in the XPS spectra to specific decomposition products. We can discount significant formation of species C_3 as likely, due to the endergonic nature of this pathway as well as the lack of any significant spectroscopic indication of Cu–CH_3 bond formation. We can further rule out C_2, as the O_2 atom is predicted by DFT to shift significantly to higher binding energies, and no such shift or new peak is observed in our XPS spectra. We can thus unambiguously assign the CH_3-A and P_1 peaks as belonging to configuration C_4. The P_2 peak can have contributions from C_1, C_5, and/or C_6/C_7 (C_6 and C_7 are predicted to be indistinguishable in XPS). The CH_3-B peak could belong to either C_1 or C_5. The remaining peaks cannot be assigned uniquely to any one species.

With these assignments, we then estimated[53] the total coverage of P-containing DMMP fragments (C_1/C_5, C_4, and C_6/C_7) from the total area of the P_1+P_2 peaks in the P 2p spectra and the corresponding attenuation of the Cu 3s peaks at each p_{DMMP} (see Supporting Information section A5 for details on the coverage calculations), and these results are plotted in Figure 9b. The total coverage of P-containing fragments increases slightly from 0.80 monolayers (ML) at $p_{DMMP} = 1 \times 10^{-7}$ Torr to 0.88 ML at $p_{DMMP} = 1 \times 10^{-4}$ Torr. These calculations do not account for the surface Cu−OCH$_3$ and O$_{lat}$−CH$_3$ methoxy groups, which should also attenuate the Cu 3s peak to some degree. Thus, these estimates should be taken as the lower limit of surface coverage, and it is not unreasonable to assume a full monolayer surface coverage when including Cu−OCH$_3$ and O$_{lat}$−CH$_3$ groups.

Multiplying the total coverage by the fraction of $P_1/(P_1+P_2)$ gives the approximate coverage of species C_4 (0.24−0.30 ML). Similarly, the coverage of P_2 is calculated and found to be relatively constant across all p_{DMMP} conditions measured. The ratio of CH$_3$-A/CH$_3$-B can be used to approximate the coverage of configurations C_1/C_5 on the surface, and thus the fraction of the P_2 peak area that corresponds to C_1/C_5 (with the remaining P_2 area corresponding to C_6/C_7). The coverage of the CH$_3$-B species is initially 0.23 ML and decreases to 0.04 ML at 1×10^{-5} Torr = p_{DMMP}. As mentioned previously, there are two extreme possible scenarios for assigning the CH$_3$-B peak:

(1) C_1 is not observable by XPS, and thus, CH$_3$-B can be assigned uniquely to C_5. As p_{DMMP} increases, all C_5 is converted to C_6/C_7 and some additional DMMP is adsorbed and converted to C_4.

(2) C_5 is not observable by XPS, and thus, CH$_3$-B can be assigned uniquely to C_1. As p_{DMMP} increases, all C_1 is converted to C_4 and/or C_6/C_7. Some additional DMMP adsorption could result in formation of additional C_4 and/or C_6/C_7.

In scenario 1, since C_5 and C_6/C_7 are all contained in the P_2 peak, the conversion of C_5 would result in no net change in the area of P_1, an increase in the area of the Cu−O−X and OCH$_3$ peaks, and a decrease in the P−OCH$_3$ peak. The formation of C_4 from additional DMMP adsorption would increase the Cu−O−X, P−OCH$_3$, CH$_3$-A, and OCH$_3$ peak areas. For scenario 2, complete consumption of C_1 while maintaining a constant coverage of P_1 requires that either all of C_1 is converted to C_6/C_7 and additional DMMP adsorption only forms C_4 or C_1 and all additional adsorbed DMMP convert to a combination of C_4 and C_6/C_7 such that the coverage of P_1 coincidentally does not change.

We cannot definitively conclude whether scenario 1 or 2 or a combination of these two scenarios is occurring, as most of the peaks in the XPS spectra arise from multiple species that lack unique spectral signatures and there is some inevitable error in the peak areas due to peak fitting (a reasonable assumption is 10−20% of the fitted peak area values). However, any of these situations would be consistent with the relative ratios of the different peaks and the trends in their areas observed as p_{DMMP} is increased. In particular, that P_2 stays relatively constant while the most dramatic increases are in P_1 and P−OCH$_3$ groups is consistent with additional formation of C_4 at higher p_{DMMP}.

As a final note, the binding energy shift for the C2 carbon atom upon movement of the O$_2$−C$_2$ methoxy group to the CuO surface (C_5, C_6, and C_7) is the only one calculated by DFT that is not consistent with our experimental observations. One possible explanation is that, if these groups are formed by a reaction with surface OH groups, they could eliminate as methanol from the surface and thus are not observed in XPS. The small concentration of gas-phase methanol evolved would also not be detectable during XPS experiments. Despite some background pressure of DMMP in the chamber during XPS experiments, the maximum total chamber pressure is still much lower than the pressure at which FTIR experiments are performed (760 Torr). This pressure difference could facilitate methanol desorption during XPS that would not be observed during FTIR. This would then explain how the total area of the Cu−O−X peak could remain constant while still allowing for additional DMMP adsorption and decomposition at higher p_{DMMP}.

5. CONCLUSIONS

We have demonstrated that adsorption and decomposition of DMMP on polycrystalline CuO occurs readily at room temperature, with the majority of the decomposition products remaining on the CuO surface. The *in situ* APXPS and DRIFTS experiments provided valuable complementary information on the surface chemistry in this study, painting a clearer picture of the reactivity of DMMP with the CuO surface than either method could have achieved on its own. Furthermore, the DFT core-level ionization and vibrational frequency calculations corroborated the experimental results, enabling assignment of specific features in the spectra to individual decomposition products.

DFT calculations indicated that oxygen vacancies on the surface are not the primary drivers of DMMP decomposition, which contrasts with our previous study of MoO$_3$.[17] This finding is corroborated by the nearly complete coverage of the surface by decomposition fragments and/or adsorbed DMMP as determined by quantitative analysis of the XPS spectra. The CuO lattice oxygen atoms play a crucial role in the formation of new chemical bonds (O$_{lat}$−CH$_3$ and O$_{lat}$−P) with the DMMP decomposition fragments. The decomposition mechanism proceeds through multiple steps involving bond breaking and formation at room temperature. Specifically, we observe significant breaking of P−OCH$_3$, PO−CH$_3$, and P−CH$_3$ bonds, the latter two of which are highly unusual for metal oxides at room temperature.

Features in the CuO photoelectron spectra that result from final state effects are affected by changes in the valence state electronic structure of the substrate due to participation of lattice oxygen atoms in the decomposition of DMMP. These changes are likely due to the strong charge transfer between the lattice oxygen atoms and the Cu 3d^9 valence ground state. Our DFT calculations do not show strong charge transfer, which calls for further investigation.

Nevertheless, the DFT-based simulations used here provide a robust description of DMMP decomposition on the CuO surface, as evidenced by the corroborating experimental results, and can aide in computational studies of other organophosph-(on)ate derivatives, including nerve agents and pesticides, on this and other metal oxide surfaces. This could be particularly beneficial in studies of the more toxic organophosph(on)ates, where experimental work can be dangerous and requires a safe, dedicated laboratory. Differences in reactivity of DMMP and, e.g., sarin could be calculated and compared, which could lend insight into the appropriateness of DMMP as a simulant molecule for CWA adsorption and decomposition on CuO. Computational screening of other metal oxides for reactivity with organophosph(on)ates would also expedite discovery of new

materials for improved CWA and pesticide/herbicide detection, sensing, and destruction.

■ ASSOCIATED CONTENT

■ AUTHOR INFORMATION

Corresponding Author

*E-mail: hbluhm@lbl.gov.

ORCID Ⓘ

Lena Trotochaud: 0000-0002-8816-3781

Ashley R. Head: 0000-0001-8733-0165

Jeffrey Long: 0000-0002-5184-5260

Michael Zachariah: 0000-0002-4115-3324

Notes

The authors declare no competing financial interest.

■ ACKNOWLEDGMENTS

■ REFERENCES

(1) Jang, Y. J.; Kim, K.; Tsay, O. G.; Atwood, D. A.; Churchill, D. G. Update 1 Of: Destruction and Detection of Chemical Warfare Agents. *Chem. Rev.* **2015**, *115*, PR1−PR76.

(2) Friboulet, A.; Rieger, F.; Goudou, D.; Amitai, G.; Taylor, P. Interaction of an Organophosphate with a Peripheral Site on Acetylcholinesterase. *Biochemistry* **1990**, *29*, 914−920.

(3) Albaret, C.; Lacoutière, S.; Ashman, W. P.; Froment, D.; Fortier, P.-L. Molecular Mechanic Study of Nerve Agent O-Ethyl S-[2-(Diisopropylamino)Ethyl]Methylphosphonothioate (VX) Bound to the Active Site of Torpedo Californica Acetylcholinesterase. *Proteins: Struct., Funct., Genet.* **1997**, *28*, 543−555.

(4) Shih, T.-M.; Kan, R. K.; McDonough, J. H. In Vivo Cholinesterase Inhibitory Specificity of Organophosphorus Nerve Agents. *Chem.-Biol. Interact.* **2005**, *157−158*, 293−303.

(5) Mondloch, J. E.; et al. Destruction of Chemical Warfare Agents Using Metal−Organic Frameworks. *Nat. Mater.* **2015**, *14*, 512−516.

(6) Bromberg, L.; Su, X.; Martis, V.; Zhang, Y.; Hatton, T. A. Self-Decontaminating Fibrous Materials Reactive toward Chemical Threats. *ACS Appl. Mater. Interfaces* **2016**, *8*, 17555−17564.

(7) Shen, Z.; Zhong, J.-Y.; Han, X.-Y.; Wang, L.-Y.; Cui, Y.; Chen, L.-K.; Zheng, Y.-C. Decontamination of Chemical Warfare Agents on Sensitive Equipment Materials Using Zr^{4+} and Ge^{4+} Co-Doped TiO_2 and Hydrofluoroether Suspension. *Chem. Eng. J.* **2016**, *302*, 111−119.

(8) DeCoste, J. B.; Peterson, G. W. Metal−Organic Frameworks for Air Purification of Toxic Chemicals. *Chem. Rev.* **2014**, *114*, 5695−5727.

(9) Morrison, R. W. *NBC Filter Performance*; ECBC-TR-135; U.S. Army Soldier and Biological Chemical Command: Aberdeen Proving Ground, MD, 2001.

(10) Wang, G.; et al. Mechanism and Kinetics for Reaction of the Chemical Warfare Agent Simulant, DMMP(G), with Zirconium(IV) MOFs: An Ultrahigh-Vacuum and DFT Study. *J. Phys. Chem. C* **2017**, *121*, 11261−11272.

(11) Ratliff, J. S.; Tenney, S. A.; Hu, X.; Conner, S. F.; Ma, S.; Chen, D. A. Decomposition of Dimethyl Methylphosphonate on Pt, Au, and Au−Pt Clusters Supported on TiO_2(110). *Langmuir* **2009**, *25*, 216−225.

(12) Zhou, J.; Ma, S.; Kang, Y. C.; Chen, D. A. Dimethyl Methylphosphonate Decomposition on Titania-Supported Ni Clusters and Films: A Comparison of Chemical Activity on Different Ni Surfaces. *J. Phys. Chem. B* **2004**, *108*, 11633−11644.

(13) Hegde, R. I.; Greenlief, C. M.; White, J. M. Surface Chemistry of Dimethyl Methylphosphonate on Rhodium(100). *J. Phys. Chem.* **1985**, *89*, 2886−2891.

(14) Gordon, W. O.; Tissue, B. M.; Morris, J. R. Adsorption and Decomposition of Dimethyl Methylphosphonate on Y_2O_3 Nanoparticles. *J. Phys. Chem. C* **2007**, *111*, 3233−3240.

(15) Chen, D. A.; Ratliff, J. S.; Hu, X.; Gordon, W. O.; Senanayake, S. D.; Mullins, D. R. Dimethyl Methylphosphonate Decomposition on Fully Oxidized and Partially Reduced Ceria Thin Films. *Surf. Sci.* **2010**, *604*, 574−587.

(16) Ma, S.; Zhou, J.; Kang, Y. C.; Reddic, J. E.; Chen, D. A. Dimethyl Methylphosphonate Decomposition on Cu Surfaces: Supported Cu Nanoclusters and Films on TiO_2(110). *Langmuir* **2004**, *20*, 9686−9694.

(17) Head, A. R.; Tsyshevsky, R.; Trotochaud, L.; Yu, Y.; Kyhl, L.; Karslıoğlu, O.; Kuklja, M. M.; Bluhm, H. Adsorption of Dimethyl Methylphosphonate on MoO_3: The Role of Oxygen Vacancies. *J. Phys. Chem. C* **2016**, *120*, 29077−29088.

(18) Ekerdt, J. G.; Klabunde, K. J.; Shapley, J. R.; White, J. M.; Yates, J. T. Surface Chemistry of Organophosphorus Compounds. *J. Phys. Chem.* **1988**, *92*, 6182−6188.

(19) Lee, K. Y.; Houalla, M.; Hercules, D. M.; Hall, W. K. Catalytic Oxidative Decomposition of Dimethyl Methylphosphonate over Cu-Substituted Hydroxyapatite. *J. Catal.* **1994**, *145*, 223−231.

(20) Ogletree, D. F.; Bluhm, H.; Hebenstreit, E. D.; Salmeron, M. Photoelectron Spectroscopy under Ambient Pressure and Temperature Conditions. *Nucl. Instrum. Methods Phys. Res., Sect. A* **2009**, *601*, 151−160.

(21) Bluhm, H.; et al. Soft X-Ray Microscopy and Spectroscopy at the Molecular Environmental Science Beamline at the Advanced Light Source. *J. Electron Spectrosc. Relat. Phenom.* **2006**, *150*, 86−104.

(22) Ogletree, D. F.; Bluhm, H.; Lebedev, G.; Fadley, C. S.; Hussain, Z.; Salmeron, M. A Differentially Pumped Electrostatic Lens System for Photoemission Studies in the Millibar Range. *Rev. Sci. Instrum.* **2002**, *73*, 3872−3877.

(23) Butrow, A. B.; Buchanan, J. H.; Tevault, D. E. Vapor Pressure of Organophosphorus Nerve Agent Simulant Compounds. *J. Chem. Eng. Data* **2009**, *54*, 1876−1883.

(24) Perdew, J. P.; Burke, K.; Ernzerhof, M. Generalized Gradient Approximation Made Simple. *Phys. Rev. Lett.* **1996**, *77*, 3865−3868.

(25) Blöchl, P. E. Projector Augmented-Wave Method. *Phys. Rev. B: Condens. Matter Mater. Phys.* **1994**, *50*, 17953−17979.

(26) Kresse, G.; Furthmüller, J. Efficient Iterative Schemes for Ab Initio Total-Energy Calculations Using a Plane-Wave Basis Set. *Phys. Rev. B: Condens. Matter Mater. Phys.* **1996**, *54*, 11169−11186.

(27) Kresse, G.; Hafner, J. Ab Initio Molecular Dynamics for Liquid Metals. *Phys. Rev. B: Condens. Matter Mater. Phys.* **1993**, *47*, 558−561.

(28) Dudarev, S. L.; Botton, G. A.; Savrasov, S. Y.; Humphreys, C. J.; Sutton, A. P. Electron-Energy-Loss Spectra and the Structural Stability

of Nickel Oxide: An LSDA+U Study. *Phys. Rev. B: Condens. Matter Mater. Phys.* **1998**, *57*, 1505−1509.

(29) Nolan, M.; Elliott, S. D. The P-Type Conduction Mechanism in Cu₂O: A First Principles Study. *Phys. Chem. Chem. Phys.* **2006**, *8*, 5350−5358.

(30) Maimaiti, Y.; Nolan, M.; Elliott, S. D. Reduction Mechanisms of the CuO(111) Surface through Surface Oxygen Vacancy Formation and Hydrogen Adsorption. *Phys. Chem. Chem. Phys.* **2014**, *16*, 3036−3046.

(31) Hu, J.; Li, D.; Lu, J. G.; Wu, R. Effects on Electronic Properties of Molecule Adsorption on CuO Surfaces and Nanowires. *J. Phys. Chem. C* **2010**, *114*, 17120−17126.

(32) Tang, W.; Sanville, E.; Henkelman, G. A Grid-Based Bader Analysis Algorithm without Lattice Bias. *J. Phys.: Condens. Matter* **2009**, *21*, 084204.

(33) Sanville, E.; Kenny, S. D.; Smith, R.; Henkelman, G. Improved Grid-Based Algorithm for Bader Charge Allocation. *J. Comput. Chem.* **2007**, *28*, 899−908.

(34) Henkelman, G.; Arnaldsson, A.; Jónsson, H. A Fast and Robust Algorithm for Bader Decomposition of Charge Density. *Comput. Mater. Sci.* **2006**, *36*, 354−360.

(35) Köhler, L.; Kresse, G. Density Functional Study of Co on Rh(111). *Phys. Rev. B: Condens. Matter Mater. Phys.* **2004**, *70*, 165405.

(36) Rusu, C. N.; Yates, J. T., Jr. Adsorption and Decomposition of Dimethyl Methylphosphonate on TiO₂. *J. Phys. Chem. B* **2000**, *104*, 12292−12298.

(37) Badri, A.; Binet, C.; Lavalley, J.-C. Use of Methanol as an Ir Molecular Probe to Study the Surface of Polycrystalline Ceria. *J. Chem. Soc., Faraday Trans.* **1997**, *93*, 1159−1168.

(38) Lamotte, J.; Morávek, V.; Bensitel, M.; Lavalley, J. C. FT-IR Study of the Structure and Reactivity of Methoxy Species on ThO₂ and CeO₂. *React. Kinet. Catal. Lett.* **1988**, *36*, 113−118.

(39) Daturi, M.; Binet, C.; Lavalley, J. C.; Galtayries, A.; Sporken, R. Surface Investigation on Ce₍ₓ₎Zr₍₁₋ₓ₎O₂ Compounds. *Phys. Chem. Chem. Phys.* **1999**, *1*, 5717−5724.

(40) Mitchell, M. B.; Sheinker, V. N.; Cox, W. W.; Gatimu, E. N.; Tesfamichael, A. B. The Room Temperature Decomposition Mechanism of Dimethyl Methylphosphonate (DMMP) on Alumina-Supported Cerium Oxide − Participation of Nano-Sized Cerium Oxide Domains. *J. Phys. Chem. B* **2004**, *108*, 1634−1645.

(41) Aurian-Blajeni, B.; Boucher, M. M. Interaction of Dimethyl Methylphosphonate with Metal Oxides. *Langmuir* **1989**, *5*, 170−174.

(42) Mitchell, M. B.; Sheinker, V. N.; Mintz, E. A. Adsorption and Decomposition of Dimethyl Methylphosphonate on Metal Oxides. *J. Phys. Chem. B* **1997**, *101*, 11192−11203.

(43) Wilmsmeyer, A. R.; Uzarski, J.; Barrie, P. J.; Morris, J. R. Interactions and Binding Energies of Dimethyl Methylphosphonate and Dimethyl Chlorophosphate with Amorphous Silica. *Langmuir* **2012**, *28*, 10962−10967.

(44) Li, Y.-X.; Schlup, J. R.; Klabunde, K. J. Fourier Transform Infrared Photoacoustic Spectroscopy Study of the Adsorption of Organophosphorus Compounds on Heat-Treated Magnesium Oxide. *Langmuir* **1991**, *7*, 1394−1399.

(45) Panayotov, D. A.; Morris, J. R. Uptake of a Chemical Warfare Agent Simulant (DMMP) on TiO₂: Reactive Adsorption and Active Site Poisoning. *Langmuir* **2009**, *25*, 3652−3658.

(46) Jiang, P.; et al. Experimental and Theoretical Investigation of the Electronic Structure of Cu₂O and CuO Thin Films on Cu(110) Using X-Ray Photoelectron and Absorption Spectroscopy. *J. Chem. Phys.* **2013**, *138*, 024704.

(47) Biesinger, M. C.; Lau, L. W. M.; Gerson, A. R.; Smart, R. S. C. Resolving Surface Chemical States in XPS Analysis of First Row Transition Metals, Oxides and Hydroxides: Sc, Ti, V, Cu and Zn. *Appl. Surf. Sci.* **2010**, *257*, 887−898.

(48) Galakhov, V. R.; et al. Interaction of Cu 3d and O 2p States in Mg₁₋ₓCuₓO Solid Solutions with NaCl Structure: X-Ray Photoelectron and X-Ray Emission Study. *Phys. Rev. B: Condens. Matter Mater. Phys.* **2000**, *62*, 4922−4926.

(49) van der Laan, G.; Westra, C.; Haas, C.; Sawatzky, G. A. Satellite Structure in Photoelectron and Auger Spectra of Copper Dihalides. *Phys. Rev. B: Condens. Matter Mater. Phys.* **1981**, *23*, 4369−4380.

(50) McIntyre, N. S.; Cook, M. G. X-Ray Photoelectron Studies on Some Oxides and Hydroxides of Cobalt, Nickel, and Copper. *Anal. Chem.* **1975**, *47*, 2208−2213.

(51) Scrocco, M. Satellite Structure in the X-Ray Photoelectron Spectra of CuO and Cu₂O. *Chem. Phys. Lett.* **1979**, *63*, 52−56.

(52) Ghijsen, J.; Tjeng, L. H.; van Elp, J.; Eskes, H.; Westerink, J.; Sawatzky, G. A.; Czyzyk, M. T. Electronic Structure of Cu₂O and CuO. *Phys. Rev. B: Condens. Matter Mater. Phys.* **1988**, *38*, 11322−11330.

(53) Newberg, J. T. Formation of Hydroxyl and Water Layers on MgO Films Studied with Ambient Pressure XPS. *Surf. Sci.* **2011**, *605*, 89−94.

(54) Thuler, M. R.; Benbow, R. L.; Hurych, Z. Resonant Photo- and Auger Emission at the 3p Threshold of Cu, Cu₂O, and CuO. *Phys. Rev. B: Condens. Matter Mater. Phys.* **1982**, *26*, 669−677.

(55) Eskes, H.; Sawatzky, G. A. Tendency towards Local Spin Compensation of Holes in the High-T_C Copper Compounds. *Phys. Rev. Lett.* **1988**, *61*, 1415−1418.

(56) Finkel'shteĭn, L. D.; Zabolotskiĭ, E. I.; Galakhov, V. R.; Kurmaev, É. Z.; Ulenbrok, S.; Bartkovski, S.; Noĭmann, M. Single-Ion Approach to the Interpretation of the X-Ray Photoelectron Spectra of the Valence Bands of Monoxides of 3d Elements. *Phys. Solid State* **1997**, *39*, 948−954.

(57) Åsbrink, S.; Norrby, L.-J. A Refinement of the Crystal Structure of Copper(II) Oxide with a Discussion of Some Exceptional E.S.D.'S. *Acta Crystallogr., Sect. B: Struct. Crystallogr. Cryst. Chem.* **1970**, *26*, 8−15.

(58) Forsyth, J. B.; Brown, P. J.; Wanklyn, B. M. Magnetism in Cupric Oxide. *J. Phys. C: Solid State Phys.* **1988**, *21*, 2917.

(59) Yang, B. X.; Thurston, T. R.; Tranquada, J. M.; Shirane, G. Magnetic Neutron Scattering Study of Single-Crystal Cupric Oxide. *Phys. Rev. B: Condens. Matter Mater. Phys.* **1989**, *39*, 4343−4349.

(60) Marabelli, F.; Parravicini, G. B.; Salghetti-Drioli, F. Optical Gap of CuO. *Phys. Rev. B: Condens. Matter Mater. Phys.* **1995**, *52*, 1433−1436.

(61) Bermudez, V. M. Quantum-Chemical Study of the Adsorption of DMMP and Sarin on Gamma-Al₂O₃. *J. Phys. Chem. C* **2007**, *111*, 3719−3728.

(62) Tsyshevsky, R. V.; Rashkeev, S. N.; Kuklja, M. M. Defect States at Organic-Inorganic Interfaces: Insight from First Principles Calculations for Pentaerythritol Tetranitrate on MgO Surface. *Surf. Sci.* **2015**, *637−638*, 19−28.

(63) Wang, F.; Tsyshevsky, R.; Zverev, A.; Mitrofanov, A.; Kuklja, M. M. Can a Photosensitive Oxide Catalyze Decomposition of Energetic Materials? *J. Phys. Chem. C* **2017**, *121*, 1153−1161.

(64) Rodriguez, J. A.; Jirsak, T.; Liu, G.; Hrbek, J.; Dvorak, J.; Maiti, A. Chemistry of No2 on Oxide Surfaces: Formation of NO₃ on TiO₂(110) and NO₂ < -> O Vacancy Interactions. *J. Am. Chem. Soc.* **2001**, *123*, 9597−9605.

(65) Panayotov, D. A.; Morris, J. R. Thermal Decomposition of a Chemical Warfare Agent Simulant (DMMP) on TiO₂: Adsorbate Reactions with Lattice Oxygen as Studied by Infrared Spectroscopy. *J. Phys. Chem. C* **2009**, *113*, 15684−15691.

(66) Henderson, M. A.; Jin, T.; White, J. M. A TPD/AES Study of the Interaction of Dimethyl Methylphosphonate with Iron Oxide (Alpha-Fe₂O₃) and Silicon Dioxide. *J. Phys. Chem.* **1986**, *90*, 4607−4611.

(67) Tesfai, T. M.; Sheinker, V. N.; Mitchell, M. B. Decomposition of Dimethyl Methylphosphonate (DMMP) on Alumina-Supported Iron Oxide. *J. Phys. Chem. B* **1998**, *102*, 7299−7302.

(68) Li, Y. X.; Koper, O.; Atteya, M.; Klabunde, K. J. Adsorption and Decomposition of Organophosphorus Compounds on Nanoscale Metal Oxide Particles. In Situ GC-MS Studies of Pulsed Microreactions over Magnesium Oxide. *Chem. Mater.* **1992**, *4*, 323−330.

(69) Peterson, G. W.; Wagner, G. W. Detoxification of Chemical Warfare Agents by CuBTC. *J. Porous Mater.* **2014**, *21*, 121−126.